Article:
Silva, S.S.A., Verth, G., Ballai, I. et al. (2024) Solar vortex tubes. III. vorticity and energy transport. The Astrophysical Journal, 975 (1). 118. ISSN: 0004-637X

https://doi.org/10.3847/1538-4357/ad781a

The Astrophysical Journal, 975:118 (14pp), 2024 November 1 https://doi.org/10.3847/1538-4357/ad781a

Solar Vortex Tubes. III. Vorticity and Energy Transport

Suzana S. A. Silva[1,2], Gary Verth[3], Istvan Ballai[3], Erico L. Rempel[4], Sergiy Shelyag[5], Luiz A. C. A. Schiavo[6], Tiago F. P. Gomes[4], and Viktor Fedun[1]
[1] Plasma Dynamics Group, School of Electrical and Electronic Engineering, University of Sheffield, Sheffield, S1 3JD, UK; suzana.silva@sheffield.ac.uk
[2] Department of Physics, Aeronautics Institute of Technology, São José dos Campos, Brazil
[3] Plasma Dynamics Group, School of Mathematical and Physical Sciences, University of Sheffield, Sheffield S3 7RH, UK
[4] Department of Mathematics, Aeronautics Institute of Technology, São José dos Campos, Brazil
[5] College of Science and Engineering, Flinders University, Tonsley, 5042, South Australia, Australia
[6] Department of Mathematics, Physics and Electrical Engineering, Northumbria University, Newcastle NE1 8ST, UK
Received 2024 July 8; revised 2024 September 1; accepted 2024 September 4; published 2024 October 29

Abstract

This study investigated the mechanisms of vorticity generation and the role of vortex tubes in plasma heating and energy transport. Vortex tubes were identified using the instantaneous vorticity deviation technique in the MURaM data set of a simulated solar plage region of the solar photosphere. Within 3D kinetic vortex tubes, the misalignment of the magnetic pressure and the inverse of the density gradient, rather than baroclinic effects, primarily drive vorticity within the tubes. During their lifetime, vortices become less dense as the Lorentz force pushes plasma outwards against pressure gradients. In the simulated upper photosphere, the Lorentz force contributes to adiabatic cooling and heating by expanding or compressing the plasma around the vortex tubes. In turn, vortex motion affects the magnetic field, enhancing current generation and intensifying the Lorentz force, which may further increase adiabatic cooling and heating. Moreover, our results confirm that vortices can significantly boost viscous and ohmic heating on intergranular scales in the photosphere. They generate more magnetic than kinetic energy, with energy transport by Poynting flux notably nonuniform and dominant at the vortex boundaries. This creates energy circulation in which the net upwards Poynting flux can enhance chromospheric plasma heating and support chromospheric temperatures.

Unified Astronomy Thesaurus concepts: Solar photosphere (1518); Solar granules (1875); Solar chromospheric heating (1987); Magnetohydrodynamical simulations (1966); Quiet Sun (1322)

1. Introduction

The solar atmosphere can support different kinds of vortices. There are the classical flow vortices where the flow shows a rotational motion (G. Haller et al. 2016), called kinetic vortices (S. S. A. Silva et al. 2021). There are also magnetic vortices, where the magnetic twist is present, and Poynting flux vortices where the energy flow follows the swirling path (S. S. A. Silva et al. 2024). All kinds of vortices are rooted along intergranular lanes, but the number of kinetic or flow vortex tubes tends to be twice as much as their magnetic counterparts (S. S. A. Silva et al. 2021). Observational analysis indicates that solar kinetic vortices cover around 3% of the photosphere (I. Giagkiozis et al. 2018), presenting a radius ranging from 310 km in granular scales up to 5 Mm in supergranular flows (I. S. Requerey et al. 2018; A.C.L. Chian et al. 2019). In realistic magnetoconvection simulations, the vortex tubes have a radius ranging from 40 to 80 km (S. S. A. Silva et al. 2020; N. Yadav et al. 2021; Y. Aljohani et al. 2022) in the lower atmosphere. Both numerical and observational investigations indicate that the magnetic field is attracted and concentrated by solar kinetic vortices (R. Attie et al. 2009; L. Balmaceda et al. 2010; S. Wedemeyer-Böhm et al. 2012; S. S. A. Silva et al. 2020; N. Yadav et al. 2021), and in turn, the flow vortices impact the geometry of field lines (S. S. A. Silva et al. 2020; A. F. Battaglia et al. 2021; N. Yadav et al. 2021; S. S. A. Silva et al. 2021). In regions where the plasma-β is equal to 1 or higher, the magnetic field lines can be twisted by the shear flows originated by intergranular flows or by the flow dynamics close to the vortex's boundary, originating the magnetic vortices. In magnetoconvection simulations, the vorticity that leads to vortex flow creation is driven by magnetic terms (S. Shelyag et al. 2012; J. R. Canivete Cuissa & O. Steiner 2020), and it is dominated by the magnetic tension in the magnetic field present in the intergranular lanes. In turn, the vortical flow motion provides magnetic helicity to the magnetic field encompassed by the vortex tube (I. N. Kitiashvili et al. 2012), confirming its role in creating larger magnetic structures from small scale magnetic elements.

Kinetic vortex tubes can reach the upper atmosphere (I. N. Kitiashvili et al. 2012; S. Wedemeyer-Böhm et al. 2012; S. S. A. Silva et al. 2020; N. Yadav et al. 2021; Y. Aljohani et al. 2022), leaving observable signatures such as chromospheric swirls (K. Tziotziou et al. 2018; J. Shetye et al. 2019; K. Tziotziou et al. 2019; I. Dakanalis et al. 2022). In investigations based on different simulation data sets, the identified flow vortices have been proven to impact distinct aspects of plasma dynamics, see, e.g., the review by K. Tziotziou et al. (2023). In the lower atmosphere, vortical motions create a plasma depletion in vortex regions, leading to a less dense plasma than their vicinity (R. Moll et al. 2011; I. N. Kitiashvili et al. 2012; N. Yadav et al. 2021; A. J. Finley et al. 2022). In the lower atmosphere, the plasma inside the vortex tubes is also cooler than their surroundings, and the vortex boundary region displays hotter regions at heights above 500 km (R. Moll et al. 2012). Flow vortices are believed to contribute to chromospheric heating as they produce enough

electromagnetic energy input to justify the observed temperatures in the upper atmosphere (S. Shelyag et al. 2011; S. Wedemeyer-Böhm et al. 2012; N. Yadav et al. 2021). The vertical component of Poynting flux created by vortices is mainly a product of the horizontal vortical motions of plasma encompassing the intense magnetic flux concentrations (S. Shelyag et al. 2012; S. Candelaresi et al. 2018), and the Poynting flux tends to be more intense around vortex tubes' boundaries (I. N. Kitiashvili et al. 2012).

The spontaneous generation of jets can be linked to vortex dynamics (S. Skirvin et al. 2023) and tends to appear around, or at the vortex boundary, whereas the center presents mostly downflows (I. N. Kitiashvili et al. 2013; S. S. A. Silva et al. 2021). This conclusion was also demonstrated by D. Kuridze et al. (2016) and H. Iijima & T. Yokoyama (2017), where they showed that the Lorentz force created by the twisted magnetic field lines can drive chromospheric jetlike features like spicules. Model simulations of vortex interaction at photospheric layers indicate that they can drive shocks (B. Snow et al. 2018) that could contribute to heating in the chromosphere. However, in realistic data sets, such shocks are only present in low or nonmagnetic field simulations (R. Moll et al. 2012; I. N. Kitiashvili et al. 2013).

In this paper, we continue the analysis presented in S. S. A. Silva et al. (2020, 2021), extending it to investigate the role of kinetic vortices in energy transport and plasma heating. We will investigate what mechanism is more efficient in generating the vorticity that leads to those vortex tubes. For simplicity, we are going to refer to kinetic vortices in this paper as just vortices. The paper is organized as follows: the numerical setup used to generate the data together with the methodology employed to identify vortices is presented in Section 2. The results are presented in Section 3 and include the analysis of the evolution of vorticity and thermal evolution inside selected vortices, the contributions of heating mechanisms, and an investigation of the sources of energy together with the investigation of the transport of energy into the upper atmosphere. Finally, the results are discussed and conclusions are presented in Section 4.

2. Methodology

The data were obtained using the MURaM code (A. Vögler et al. 2005), which performed realistic MHD simulations of solar plage conditions with the net vertical magnetic field of 200 G. The rectangular domain consists of $960 \times 960 \times 160$ grid points, covering 1.6 Mm in the vertical direction and 24 Mm in x- and y-directions. The simulated visible surface at $z = 1.0$ Mm, approximately corresponding to optical depth $\tau = 1$, is 600 km below the numerical domain upper boundary. For clarity, we introduce the height above the surface, H, which is defined as $H = 0.0$ Mm at $z = 1.0$ Mm in the computational domain. The resolution of the simulation is enough to cover the convective spatial scales in the lower atmosphere. The vertical domain extends up to the temperature minimum region in the lower chromosphere. A nonadiabatic equation of state is used in this simulation based on tabulated functional dependence of pressure and temperature on density and internal energy per unit volume. For this simulation set, the physical resistivity is set to zero, and the numerical resistivity is based on a local hyperdiffusivity scheme, being close to zero in smooth regions. In the regions of high gradients of magnetic field, it will be sufficient to stabilize the numerical scheme. In our simulation, the effect of resistivity was not taken into consideration as previous studies showed that the resistivity tends to be important on scales much smaller than the ones resolved by this simulation (M. C. M. Cheung & R. H. Cameron 2012; E. Khomenko et al. 2014). And even for such scales, the neglect of resistivity would only introduce small percentage changes in the thermodynamic structure of quiet-Sun magnetic features (M. C. M. Cheung & R. H. Cameron 2012) and an underestimation of the vortex mixing properties (J. Kleimann & G. Hornig 2001), which does not affect our analysis. Further information on the numerical implementation of the nonideal equation of state can be found in the study by A. Vögler et al. (2005), and this particular simulation is described in more detail in S. S. A. Silva et al. (2020) and Y. Aljohani et al. (2022).

Our analysis focuses on a region consisting of 240×240 grid points, previously analyzed by S. S. A. Silva et al. (2020). We investigate the same vortices that were identified and studied by S. S. A. Silva et al. (2020) using the instantaneous vorticity deviation (IVD) technique (G. Haller et al. 2016), based on the following expression:

$$\mathrm{IVD}(x, t) \coloneqq |\omega(x, t) - \langle \omega(t) \rangle|. \quad (1)$$

Here, x is a position vector, $\omega = \nabla \times v$ is the vorticity, v is the velocity, and $\langle \cdot \rangle$ denotes the instantaneous spatial average. The vortex boundary at each fixed height layer in the photosphere is the given by the outermost convex closed contour of the IVD field computed for that height level (G. Haller et al. 2016; S. S. A. Silva et al. 2020). The physical meaning of the boundary, as defined by G. Haller et al. (2016), is that the particles along the vortex boundary present the same intrinsic rotation rates. The 3D vortex tube is constructed by calculating the IVD at each height level above the simulated solar surface and interpolating among the closed contours encompassing the vortex center at each height. The complete description of the construction of the vortex tubes can be found in S. S. A. Silva et al. (2020).

3. Results

We analyzed vorticity generation, plasma temperature evolution, and energy transport using the same vortex tubes that were previously identified by S. S. A. Silva et al. (2020). Figure 1 displays a close view of the analyzed region at $t = 0$ s where the lower part of the domain ($z \leqslant 1.0$ Mm) is colored by the z-component of the velocity field, and the numbers label the coherent vortices according to S. S. A. Silva et al. (2020). The velocity field lines of all detected vortices are shown in orange and green and were traced from points within the vortex boundary. Here, the green color denotes all the vortices that remained coherent, and in orange, we show the vortex tubes that lost coherence by merging or decaying during the analyzed time interval of 40 s. The blue areas indicate regions where plasma temperature varies from 2080 to 3500 K for the height range $z \geqslant 1.2$ Mm. The red areas indicate the hotter plasma regions, where temperatures vary from 5500 to 6500 K for that same height range. The vortices are located between the hotter and colder plasma regions, and that kind of temperature distribution is mainly observed along the intergranular lanes where the vortices are found.

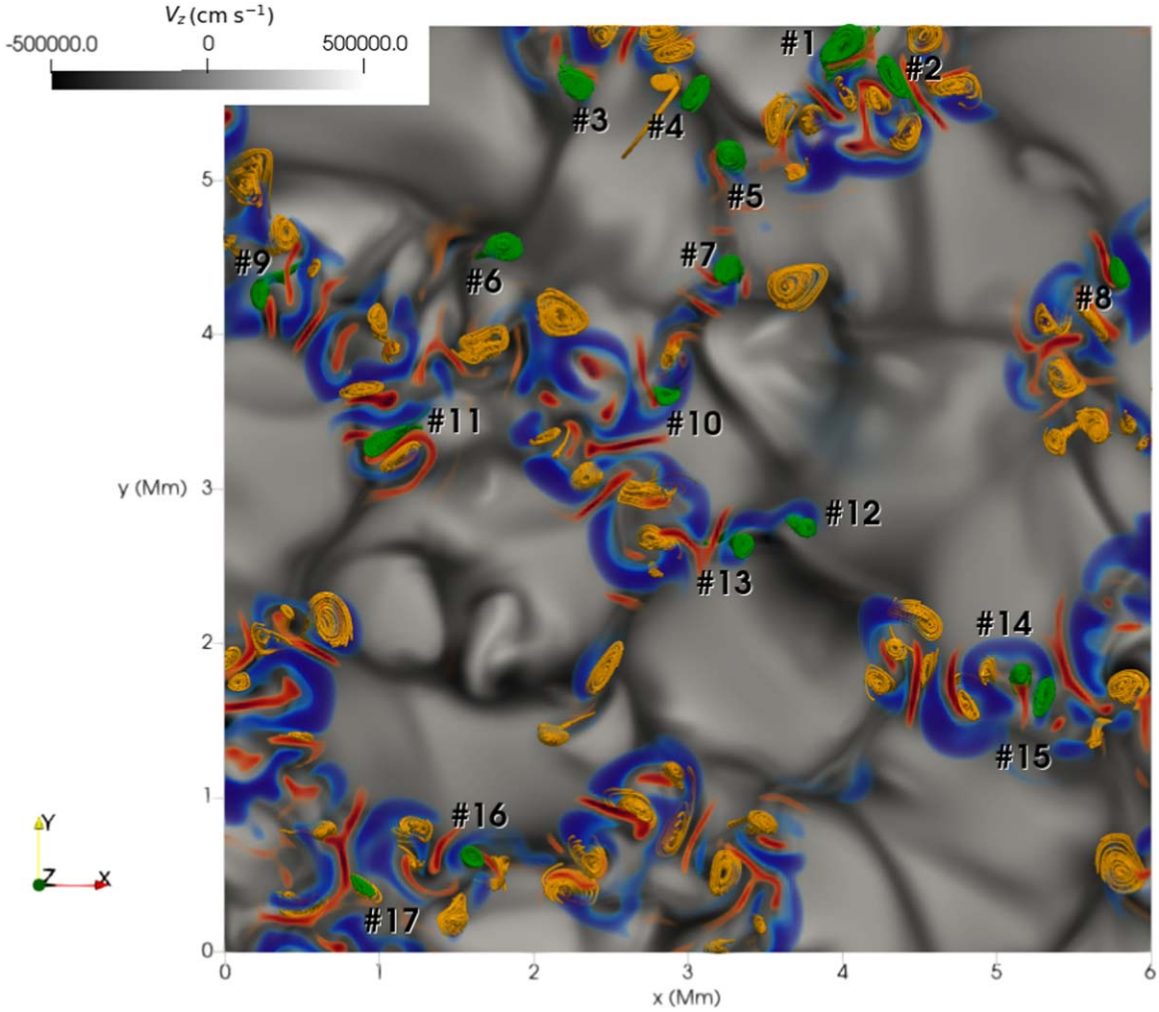

Figure 1. Close view of the simulation box at $t = 0$ s. For $z \leqslant 1.0$, the surface is colored by the z-component of the velocity field. The velocity field lines are shown in orange and green and were traced from points within the vortex boundary for every vortex detected at $t = 0$ s. The green velocity fields indicate the selected vortices. The red (blue) areas depict regions where the temperature ranges from 5500 to 6000 K (2080–3500 K).

3.1. Vorticity

The vorticity can be affected by strong pressure and density gradients, which might be present in the domain as indicated by the high-temperature gradients depicted in Figure 1. To properly evaluate the main driver of vorticity inside the vortex tubes, we write the vorticity equation in terms of nonmagnetic and magnetic terms (S. Shelyag et al. 2011):

$$\rho \frac{D}{Dt}\frac{\boldsymbol{\omega}}{\rho} = \underbrace{(\omega \cdot \nabla)\boldsymbol{v}}_{T1} \underbrace{-\nabla\frac{1}{\rho} \times \nabla p}_{T2} \underbrace{-\nabla\frac{1}{\rho} \times [\nabla p_m - (\boldsymbol{B} \cdot \nabla)\boldsymbol{B}]}_{T3} + \underbrace{\frac{1}{\rho}\nabla \times [(\boldsymbol{B} \cdot \nabla)\boldsymbol{B}]}_{T4}. \quad (2)$$

The four terms labeled as $T1$, $T2$, $T3$, and $T4$ on the right-hand side of Equation 2 are connected to the physical mechanisms responsible for generating vorticity according to our MHD model. The vortex tilting term, $T1$, appears due to the flow velocity gradients and acts to incline the vorticity vector field. The second term, $T2$, is the baroclinic term, and it generates vorticity due to the presence of pressure and density gradients, which are perpendicular in the flow. The magnetic baroclinic term, $T3$, is responsible for vorticity generation due to the presence of magnetic pressure, p_m, and magnetic field gradients not aligned with the density gradient. More specifically, the quantity in square brackets accounts for the deviation of the current magnetic field configuration from a potential field. Finally, the term $T4$ represents the vorticity generation due to the magnetic tension.

To analyze the vorticity evolution along the radial direction, we select three vortices, #7, #8, and #12, which summarize the distinct behavior found for the detected vortices, and which preserve their vertical length during the time of the analysis. We follow the methodology developed by S. S. A. Silva et al. (2020) to analyze the averaged radial profile of the selected vortices, describing the changes in the plasma from the vortex' center to its boundary as a function of the radius, r. The value of r varies for each point along the vortex boundary (i.e., each vertex); thereby, we set a grid with 10 equally spaced points along the line connecting the center and the vertex. Then, we normalize the distance from those grid points to the vortex center, $r = 0$, by the actual distance of the boundary point to the center, R. At each height level, the general tendency of the vortex radial profile is obtained by averaging the profile along the azimuthal direction

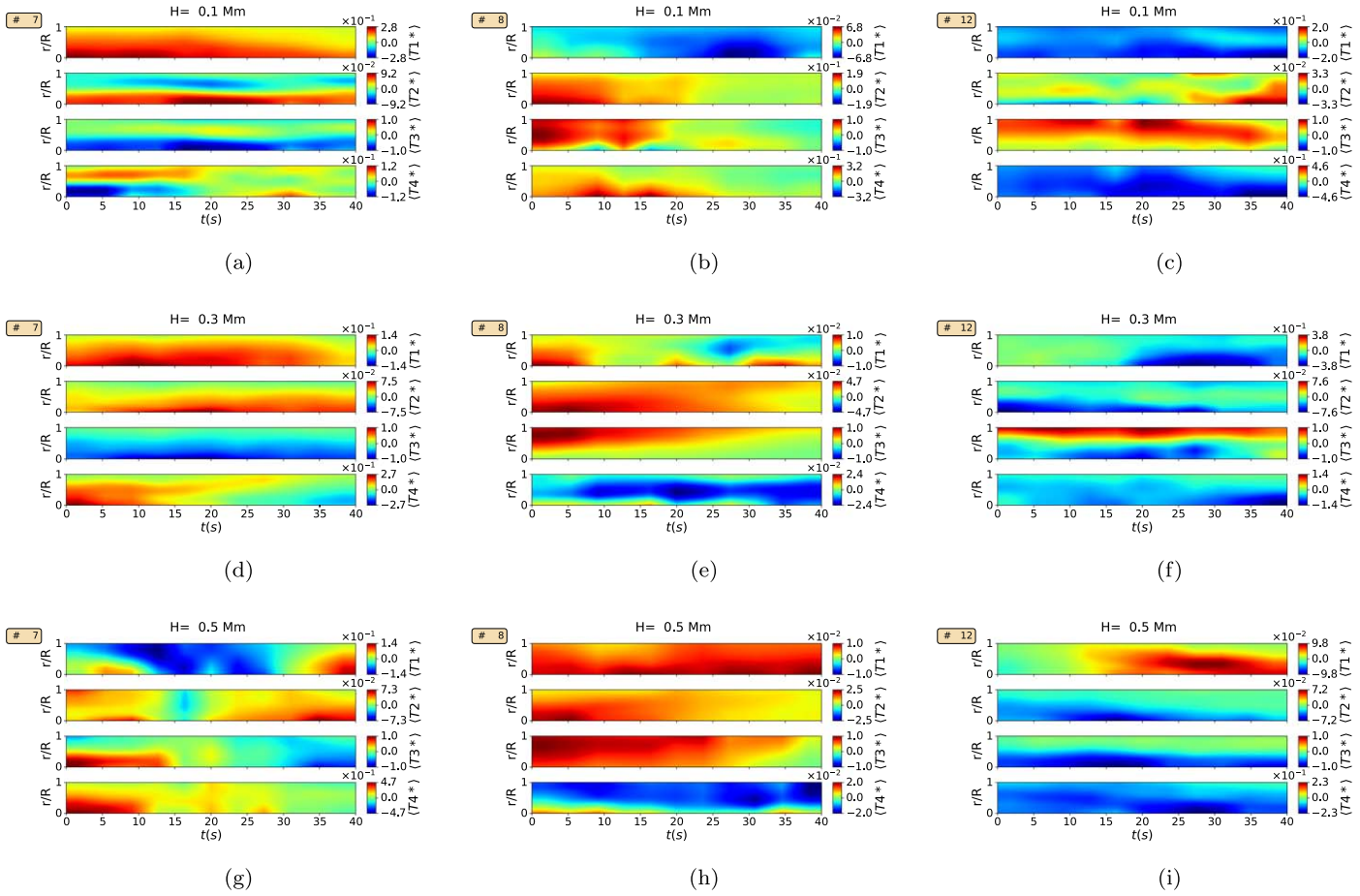

Figure 2. The average $T1$, $T2$, $T3$, and $T4$ terms normalized by $T3$ along the vortex radius from the center, $r = 0$, to the boundary $r = R$. The radial profiles are shown for vortices #7 (a), (d), (g), #8 (b), (e), (h), and #12 (c), (f), (i) at different heights: $H = 0.1$ Mm (a), (b), (c); $H = 0.3$ Mm (d), (e), (f); $H = 0.5$ Mm (g), (h), (i).

Figure 2 shows the average radial profile evolution of the vorticity terms normalized by $T3$ for the selected vortices, #7 (first column), #8 (second column), #12 (third column), at three different heights: $H = 0.1$ Mm (panels (a), (b), and (c)); $H = 0.3$ Mm (panels (d), (e), and (f)); and $H = 0.5$ Mm (panels (g), (h), and (i)). For all the investigated vortices, the main contribution to the vorticity evolution is coming from the magnetic terms, $T3$ and $T4$. This conclusion can be readily understood, as the vortices are found in regions with low plasma-β (S. S. A. Silva et al. 2021), and, thereby, the dynamics is driven mainly by the magnetic field. The main contribution comes from the magnetic baroclinic term in the vortex, $T3$. The high magnetic field concentration by the vortices leads to low values of the magnetic tension as the vortex motion can only slightly bend the magnetic field lines, and therefore, $T4$ will have lower values than $T3$. In fact, vortex #12 is the one presenting higher values for $T4$, and it is also the vortex with a weaker magnetic field and displaying more twisted magnetic field lines (S. S. A. Silva et al. 2020) and, thereby, higher magnetic tension.

The net contribution to vorticity from each term can change its sign both in time and within the vortex. Such changes are due to vorticity being generated in opposite directions by one of the terms in Equation (2); that means a term can modify its role in the vorticity evolution, going from helping the vortex development to contributing to the vorticity decay, most likely ultimately leading to vorticity oscillations in time (see, e.g., Y. Yuan et al. 2023). By comparing the terms in Figure 2, we can see that the mechanisms represented by the terms in Equation (2) will not necessarily contribute to vorticity in the same direction. Thereby, the analyzed vorticity-generating processes could actually hinder vortex formation in cases where the terms would be around the same order of magnitude. As the vortices are found in low plasma-β regions, the input from the magnetic pressure gradient in the $T3$ term tends to overcome the contributions from magnetic tension. Thereby, the vorticity equation inside the vortex tubes can be simplified to

$$\rho \frac{D}{Dt}\frac{\omega}{\rho} \approx -\nabla\frac{1}{\rho} \times \nabla p_m. \tag{3}$$

In other words, the vorticity evolution inside the vortex tubes in the photosphere is maintained by the misalignment between the gradients of the inverse density and magnetic pressure. Such a mechanism is responsible then for creating the vorticity that leads to a lasting plasma rotation, i.e., strong and coherent vortices, within narrow vertical tubes in this simulation. In cases where the magnetic field in the numerical model is 10 times weaker than the one applied in this simulation set, e.g., (I. N. Kitiashvili et al. 2013), the vorticity generation by $T2$ might become dominant, and the magnetic field can act to suppress the vorticity. In such cases, the approximation in Equation (3) would no longer represent the vorticity evolution inside the vortex tubes.

3.2. Thermal Evolution inside Vortices

The density plays an essential role in both hydrodynamic and magnetic terms in the vorticity evolution (Equation (2)). To understand the density evolution inside of vortices, we analyze how the density and also pressure and plasma temperature are, on average, distributed in the radial direction of vortices as a function of time. First, to evaluate how the temperature gradients impact the thermal evolution inside a vortex, we investigate the temperature at the vortex center as a function of height and time at three different times: $t1 = 0$ (red lines), $t2 = 20$ s (green lines), and $t3 = 40$ s (blue lines), which are depicted in Figures 3 and 4. For some vortices, the height range of the vortex center varies in time as the vortex grows or shrinks along the vertical direction. In Figures 3 and 4, the temperature evolution at the vortice's centers was classified into two distinct behaviors: temperature generally decreasing ("cold vortices" depicted in Figure 3) or increasing ("hot vortices" shown in Figure 4). The majority of detected vortices can be categorized as cold vortices, and their centers tend to cool down as a function of time and height for the analyzed time interval. In the case of hot vortices, the behavior is mixed, but the final temperature at their centers will be higher for most of the vortex height range. Due to the large temperature gradients found in the vortex region, some of the plots in Figures 3 and 4 present a lot of oscillations for the temperature as a function of height. Figures 3(j) and 4(i) display the average behavior of plasma temperature at the center of the vortices as a function of the height inside the vortex tube. The height, h, is subtracted by the height of the vortex base, h_0, and normalized by the vertical length, L, of the vortex tube. The temperature at the center is normalized by the temperature at the vortex base, T_b. The centers of cold vortices tend to present a linear decay of the center temperature, with up to around 20% colder in the upper part of the vortex. However, the difference between the temperature at the vortex top and base tends to decrease as a function of time. On the other hand, the hot vortices present mostly temperature growth as a function of height, with temperatures around 15% higher in the upper part of the vortex. As the vortex evolves, the temperature differences tend to increase indicating, in general, a hotter center as a function of height. For both hot and cold vortices, the plasma temperature profile at the center indicates that the vortices cool down at distinct rates for different heights.

The average radial profile evolution of density, temperature, and pressure for the three vortices for a total time of 40 s is shown in Figure 5. In general, the density, temperature, and pressure tend to display the same average spatial distribution across the vortical motion as a function of time. Therefore, the gradients of pressure and density in the radial direction are aligned inside the tube, which can explain the low contributions from the baroclinic term to vorticity observed in Section 3.1. Vortices #7 (Figures 5(a), (d), (g)), and #12 (Figures 5(c), (f), (i)) exhibit lower values for density, temperature, and pressure at their centers compared to their boundary, and vortex #8 displays an opposite behavior, with its centers presenting, on average, higher values than the boundary. For almost all selected height levels, the density tends to decrease in time for vortices #7 and #12, indicating that in those vortices a mechanism might be pushing the plasma out of the vortex region. The temperature inside those vortices also tends to decrease as a function of time; therefore, the depletion of plasma is most likely linked to the lower temperatures. Both vortices #7 and #12 were classified as cold vortices; in Figure 3, they only display temperature increases in regions where the density is also increasing: the upper part of the vortex #7 and the boundary of vortex #12. Vortex #8 is classified as a hot vortex, and it also exhibits average higher temperatures along the radial direction. The correlation between high average density and plasma temperature is only observed for the lower part of vortex #8. For the other parts of this particular vortex, there is an increase in temperature, but the average plasma density is diminishing as a function of time whereas the pressure is increasing.

The density evolution inside vortices #7 and #12 indicates a mechanism that is depleting the plasma in the vortex region, leading to an averaged less dense vortex. For these vortices, the plasma pressure tends to be, on average, lower at the center, which suggests that the force responsible for pushing out plasma and decreasing the vortices' density is not the plasma gradient force, which is acting in the opposite direction, i.e., from the boundary toward the center. This is confirmed by Figure 6 where we see the direction of the Lorentz force acting in the region of the selected vortices. Figure 6, displays x–y planes as colored by T at $z = 1.1$ Mm (a)–(c), $z = 1.3$ Mm (d)–(f), and $z = 1.5$ Mm (g)–(i) at the initial time of the analysis. The darker lines are tangent to the velocity field along the plane, and they were obtained using the line integration convolution (LIC; B. Cabral & L. C. Leedom 1993). The vortex boundary at each height level is represented by a white curve, which is not necessarily well aligned with the LIC. The reason for that is that the vortex detection technique employed, IVD, considers all three components of the velocity field, whereas the LIC is obtained only from the horizontal velocity. Figure 6 shows that the vortices influence both hotter and colder plasma regions, attracting them into the vortex tubes. Inside the vortex tubes, there seems to be two main effects from Lorentz force. For vortices presenting an average density drop, as vortices #7 and #12, the Lorentz force acts only by pushing plasma through the vortex. On the other hand, in the vortices experiencing density enhancement, the Lorentz force converges in a region encompassed by the boundary, as seen for vortex #8 (e), (h) and the upper part of vortex #7 (g) from the blue to red (and hotter) regions encompassed by the vortex boundary. Such behavior is also observed for all the regions where the vortices appear in the simulation domain. Thereby, the Lorentz force seems to contribute to plasma expansion as it pushes plasma out of certain regions, and it also leads to compression, indicated by the confluence of Lorentz force vectors. Comparing the plasma temperature distribution in the panels of Figure 6, there seems to exist a correlation between regions experiencing expansion (compression) due to Lorentz force and colder (hotter) plasma temperatures. Therefore, such results indicate that, inside and outside the vortex region, the Lorentz force affects the density distribution, and it does work on the plasma, leading to adiabatic cooling (heating).

3.3. Energy Generation and Transport

To gain further insight on the main energy source inside vortices, we calculated the radial profiles for the magnetic, kinetic, and internal energies, which are displayed in Figure 7. Except for the boundary region, the kinetic energy, E_k, tends to mostly experience small variations in time. By comparing with Figure 5, the variations in kinetic energy follow the density trend, but are either smaller or greater than the differences

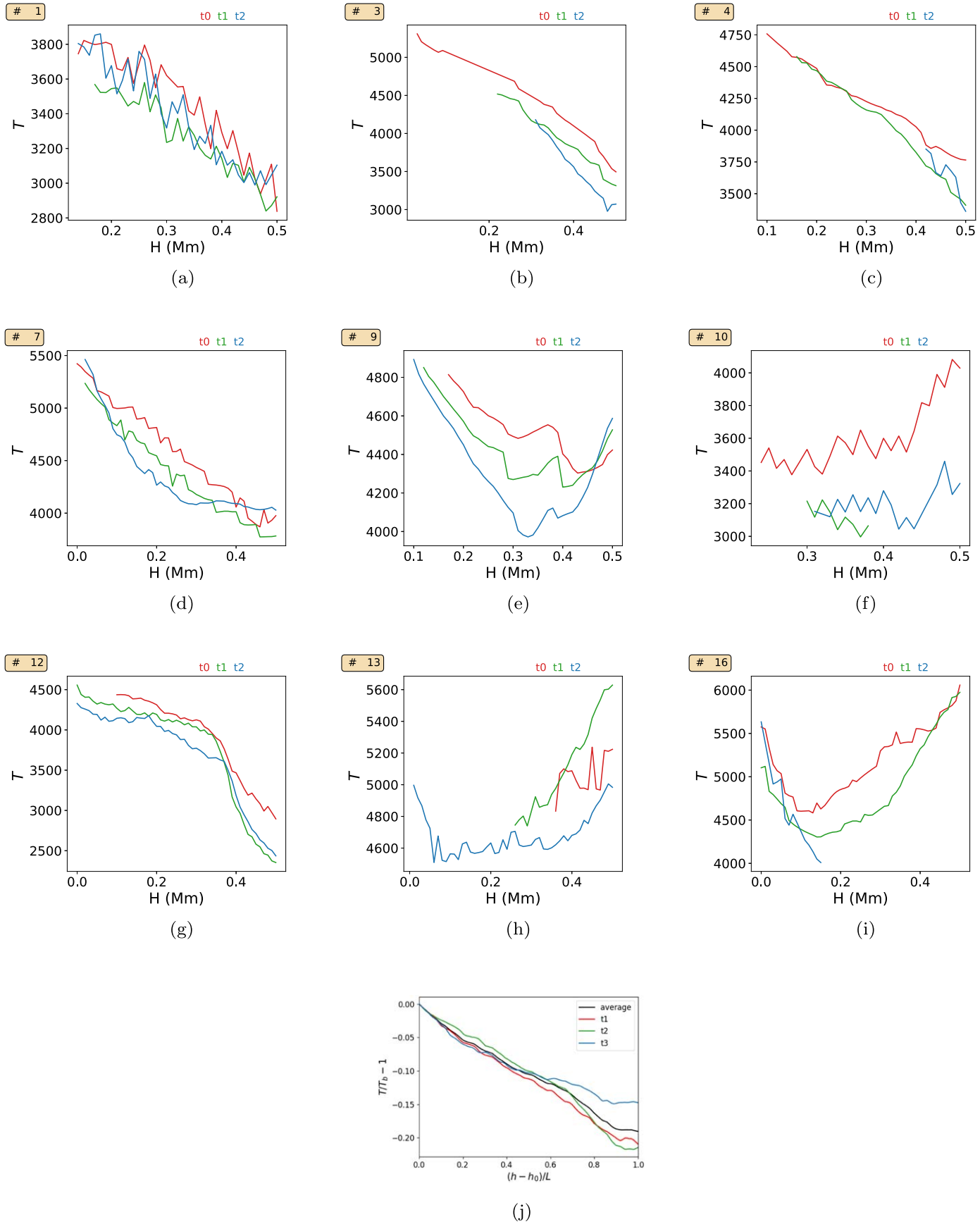

Figure 3. Average temperature at the vortex center as a function of height. The red lines are for the initial time $t0 = 0$, the green lines are for $t1 = 20$ s, and the blue lines are for $t2 = 40$ s. (a)–(i) Temperature at the center of the detected cold vortices; (j) the temperature is normalized by the temperature at the base of the vortex, T_b, and the height, h, is subtracted by h_0, which is the distance from the base of the vortex to the simulated surface, and normalized by the vertical length of the vortex, L.

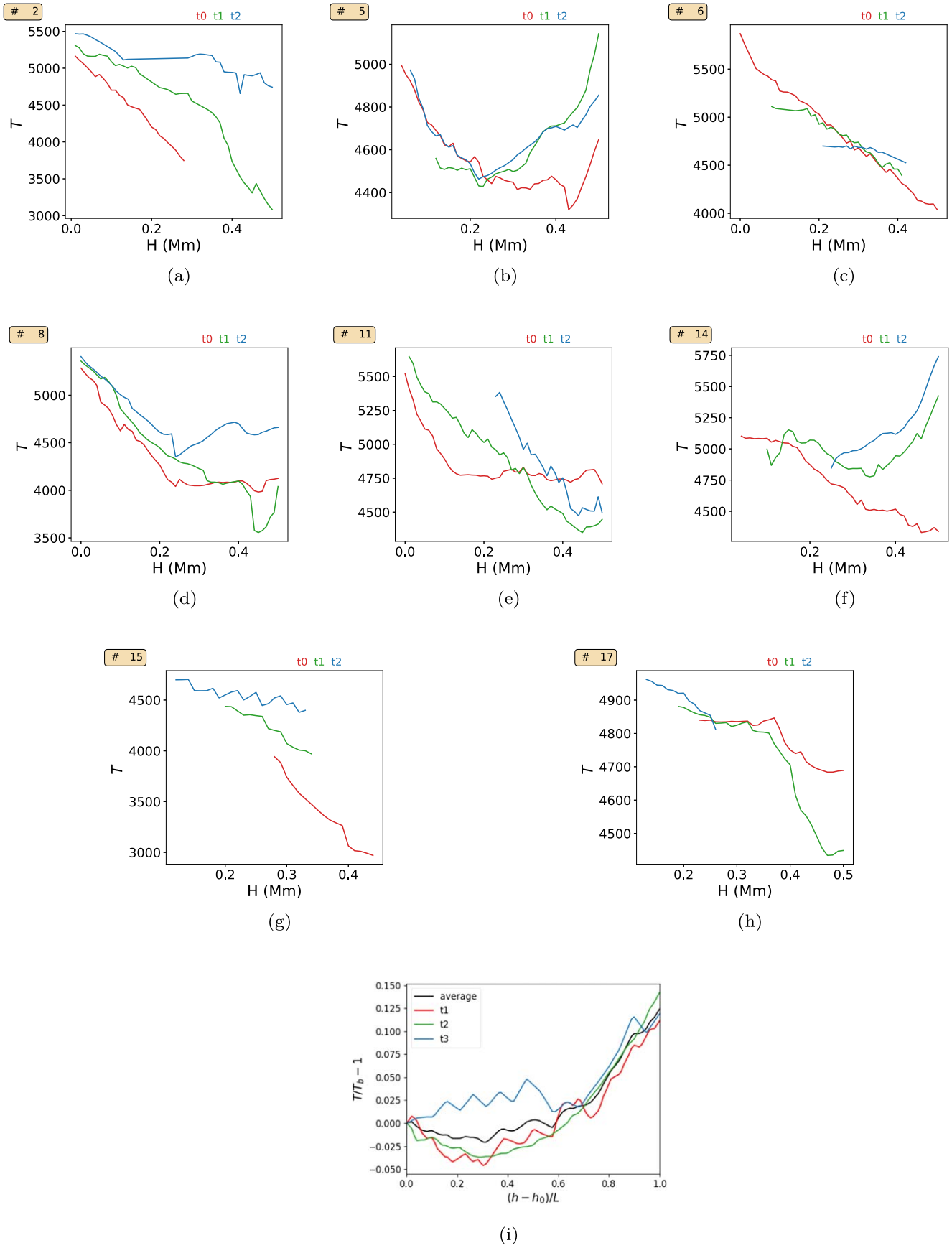

Figure 4. Same as Figure 3, but here, we show the results for the hot vortices.

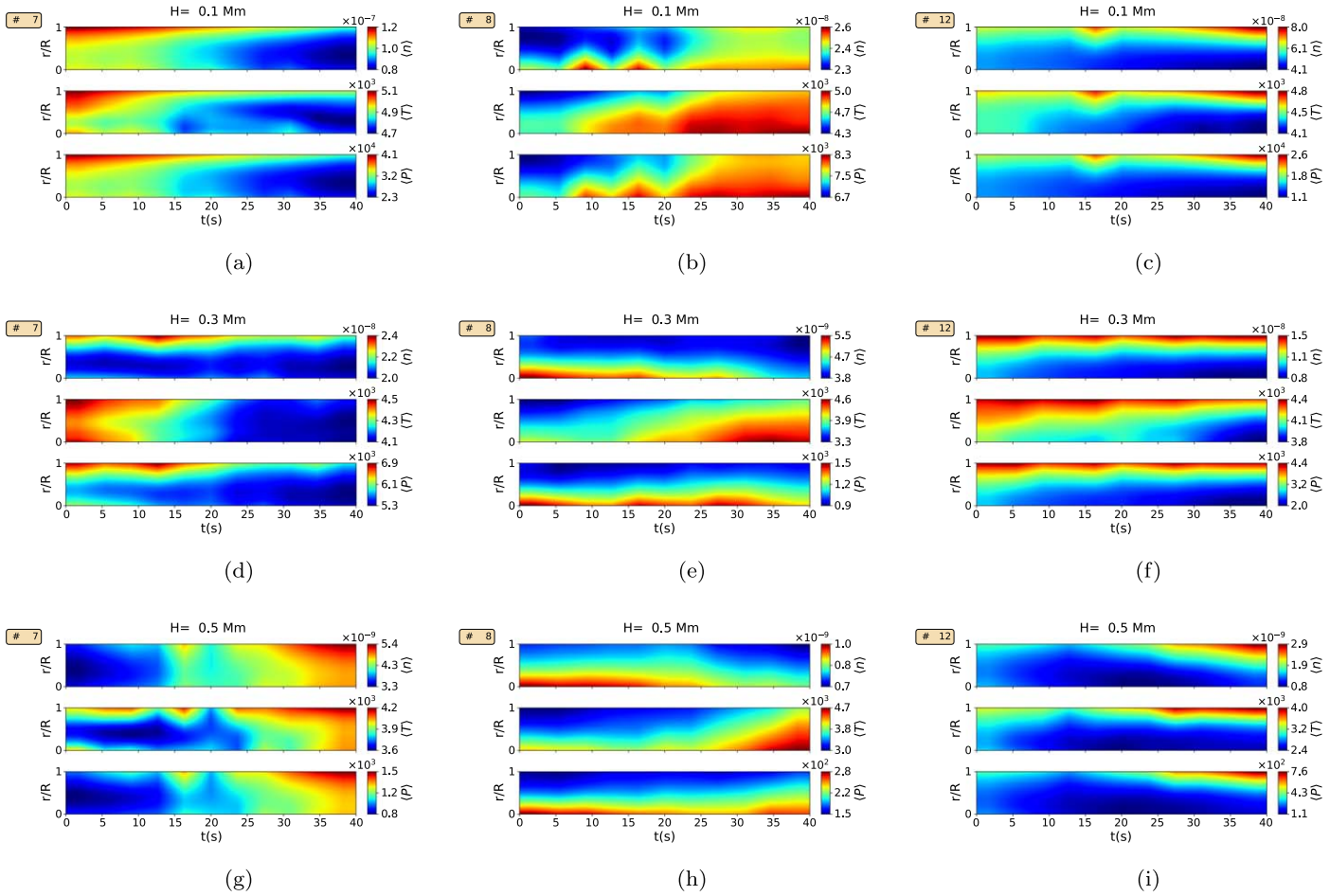

Figure 5. The average density, temperature, and pressure along the vortex radius from the center, $r = 0$, to the boundary $r = R$. The radial profiles are shown for vortices #7 (a), (d), (g), #8 (b), (e), (h), and #12 (c), (f), (i) at different heights: $H = 0.1$ Mm (a), (b), (c); $H = 0.3$ Mm (d), (e), (f); and $H = 0.5$ Mm (g), (h), (i).

found for the plasma density, indicating that the vortices are undergoing acceleration/deceleration processes.

For most height levels, the kinetic energy of vortices #7 and #8 is decreasing at the boundary, and vortex #12 presents an opposite trend, with a general tendency of increasing E_k far from the vortex center. Therefore, while vortices #7 and #8 are slowing down the rotational motion, vortex #12 is increasing its tangential speed as already indicated in S. S. A. Silva et al. (2020).

All the selected vortices tend to display the growth of magnetic energy, E_m, with vortex #8 presenting higher values of E_m.

Vortices #7 and #12 show an increase of E_m up to about 20%. On the other hand, vortex #8 displays smaller increments, except for $H = 0.1$ Mm, where it experiences losses of around 7%. The ratio E_k/E_m shows that the vortices encompass more magnetic than kinetic energy. In the vortices with higher magnetic energy, #7 and #8, the ratio tends to mostly decrease as a function of time while for vortex #12 the ratio increases but remains always smaller than unity inside the vortex tube. Thereby, the average radial profile of E_k/E_m strongly indicates the role of the vortices as a source of magnetic energy.

The internal energy, E_i, of the vortices is higher around the middle horizontal cross section of the tubes, $H = 0.3$ Mm, and it is lower closer to the simulated surface, $H = 0.1$ Mm. The variation of internal energy as a function of height in Figure 7 indicates energy transport within the vortex tubes. When the profile of E_i correlates to the temperature changes, it indicates those variations in E_i are likely due to plasma heating. When there is no correlation, the changes of E_i come from work exerted on plasma.

3.4. MHD Poynting flux

The magnetic energy created by the vortices, Figure 7, can be carried by the vortical flow as described by the MHD Poynting flux,

$$\boldsymbol{S} = \frac{1}{4\pi}[\boldsymbol{B} \times (\boldsymbol{v} \times \boldsymbol{B}) - \eta \boldsymbol{B} \times (\nabla \times \boldsymbol{B})],$$

where B is the magnetic field vector, v is the velocity field vector, and η is the resistivity (also known as the Spitzer resistivity). As the resistivity, η, is set to zero in this simulation, there is no contribution from the resistive term, and we can use the ideal MHD Poynting flux,

$$\boldsymbol{S} = \frac{1}{4\pi}\boldsymbol{B} \times (\boldsymbol{v} \times \boldsymbol{B}). \quad (4)$$

Figures 8(a), (b), (c) depict a close view of the selected vortex tubes at $t = 0$ s. The tubes are crossed by x–y planes colored by the vertical Poynting flux, S_z, and the arrows depict the orientation of the horizontal part of the velocity field. The lower panels, Figures 8((d)–(l)), display the same x–y planes as

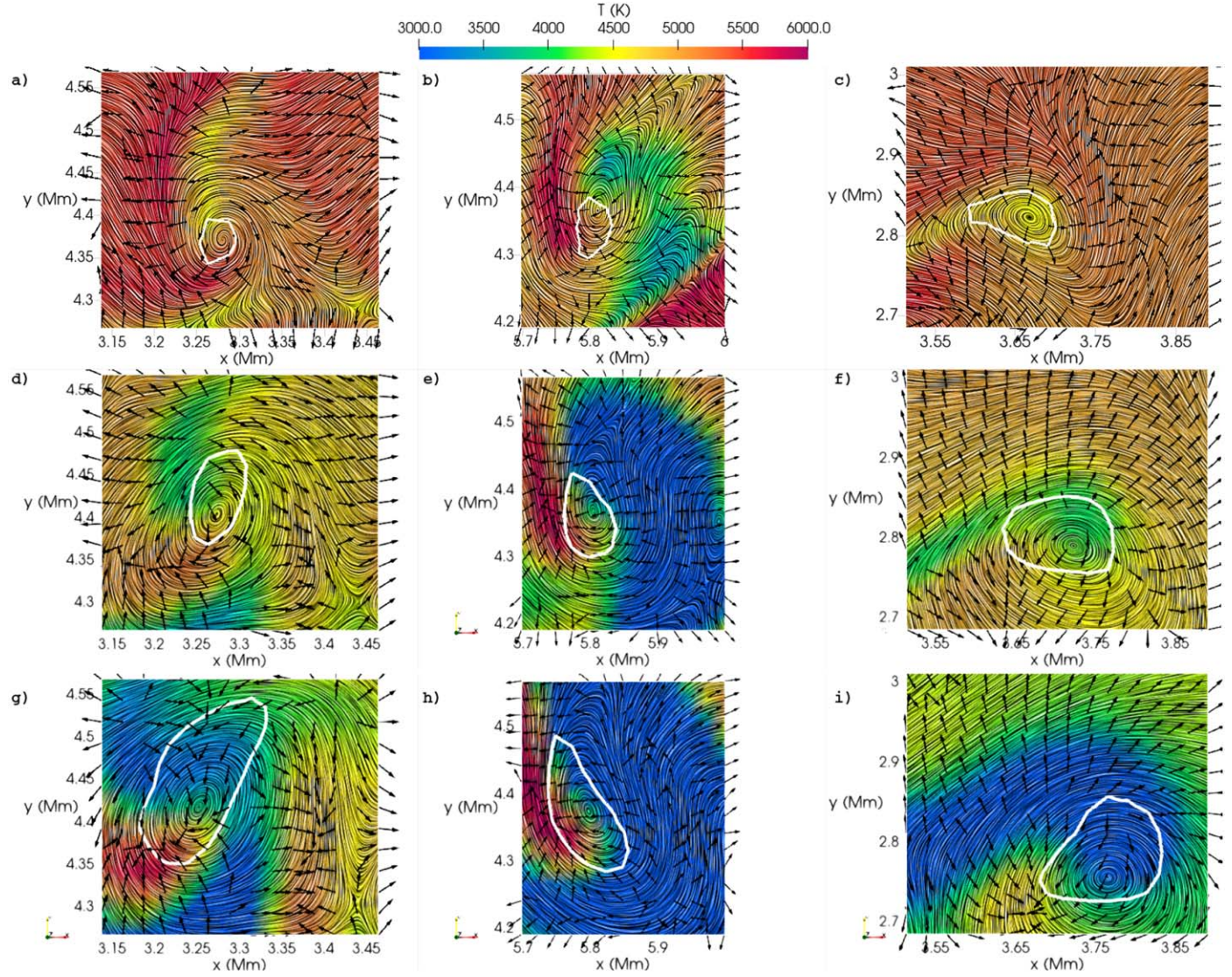

Figure 6. Close view of vortices: #7 (a), (d), (g),#8 (b), (e), (h), #12 (c), (f), (i) at $t = 0$ s. Panels (a), (b), and (c): The vortex tube is crossed by x–y planes colored by the temperature, and the black arrows provide the orientation of the horizontal component of the Lorentz force. The velocity field direction is indicated by the LIC, and the white contour depicts the vortex boundary at each height level. Panels (a)–(c): x–y plane placed at $z = 1.1$ Mm (d)–(f); $z = 1.3$ Mm (g)–(i); and $z = 1.5$ Mm (j)–(l).

panels (a)–(c) colored by S_z at $z = 1.1$ Mm (d)–(f), $z = 1.3$ Mm (g)–(i), and $z = 1.5$ Mm (j)–(l), and the LIC indicate the direction of the horizontal velocity field. In summary, in the vortex and its surrounding, the plasma motion leads not only to up or down flows, but rather to a mixture of both in the vertical direction, with a positive or negative net vertical component of the Poyting flux, S_z. Nevertheless, considering the whole simulation domain, the average net S_z transported by the detected vortices is positive, $S_z = 1.36 \times 10^8$ erg s^{-1} cm^{-2}. By comparing Figures 6 and 8, there seems to be a correlation between hotter plasma regions and areas with positive vertical Poynting flux.

To evaluate the contributions of horizontal plasma motions, we followed S. Shelyag et al. (2012) and wrote the z-component of Poynting flux as $S_z = S_{z,V} + S_{z,H}$, where the terms two are given by

$$S_{z,V} = v_z(B_x^2 + B_y^2), \tag{5}$$

$$S_{z,H} = -B_z(v_x B_x + v_y B_y). \tag{6}$$

The term $S_{z,V}$ is the Poynting flux generated by vertical plasma motions, and $S_{z,H}$ is produced by horizontal plasma motions. Figure 9 shows the time evolution of average radial profiles of $S_{z,V}$, $S_{z,H}$, and S_z for vortices #7 (left column), #8 (middle column), and #12 (right column) at $H = 0.1$ Mm (a), (b), (c); $H = 0.3$ Mm (d), (e), (f); and $H = 0.5$ Mm (g), (h), (i). For this analysis, we considered the regions outside the vortex up to 2 times the vortex radius, $r/R = 2$. For all the vortices, the main contribution to S_z comes from the Poynting flux generated by horizontal motions. The net vertical Poynting flux tends to be stronger at the boundaries, and it can display changes in signs within the region encompassed by the vortex. For example, in vortex #7 at $z = 1.3$ Mm and $z = 1.5$ Mm, there is a downflow of energy at certain times closer to the vortex center, $r/R = 0$, and upflows around the boundary region. The orientation of the net vertical Poynting flux also changes in time as depicted for the selected vortices, especially at $z = 1.5$ Mm. Thereby, the vortices can be considered as a very dynamic energy channel, and their contribution to magnetic energy transport is affected

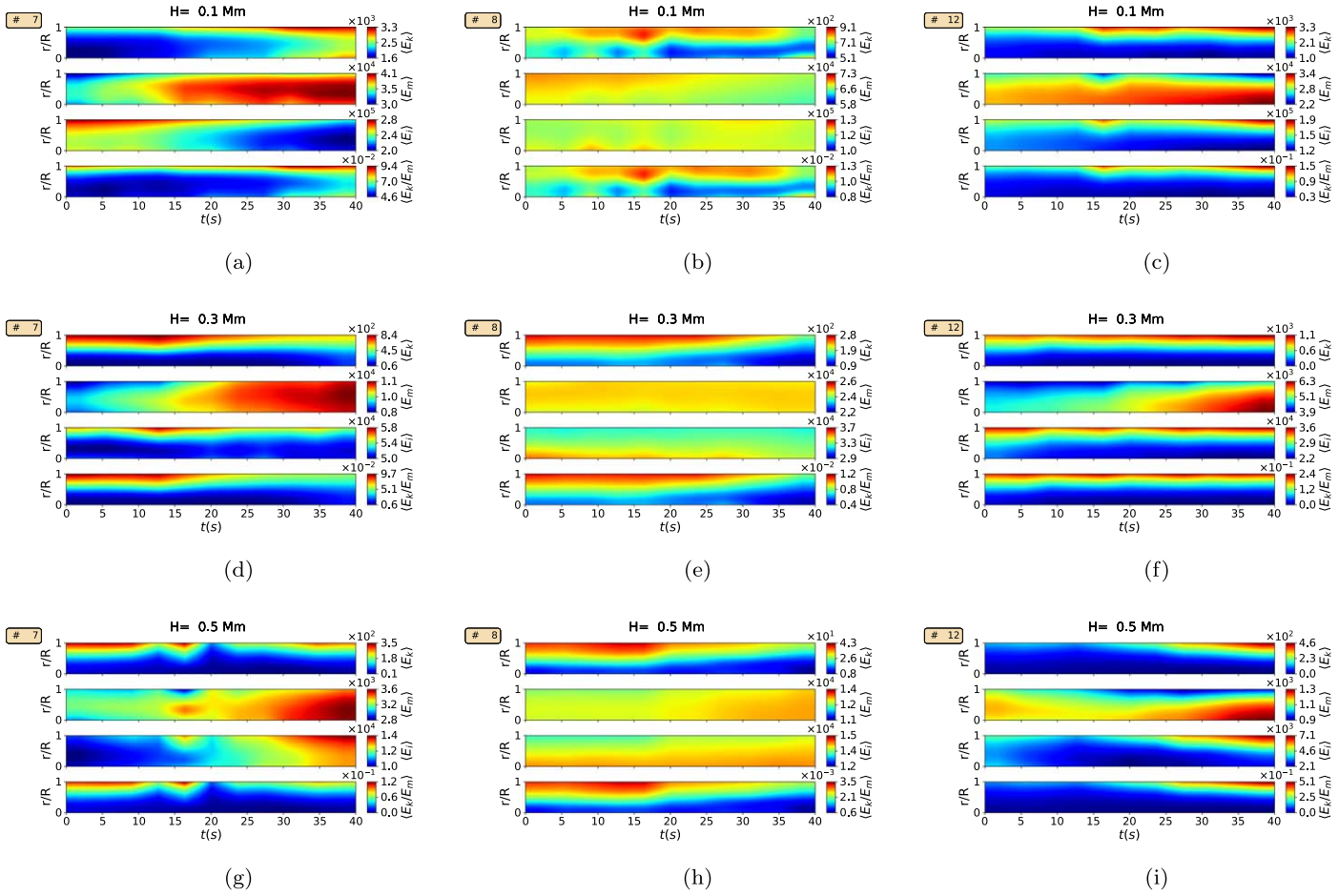

Figure 7. The angular averages of kinetic $\langle E_k \rangle$, magnetic $\langle E_m \rangle$, internal $\langle E_i \rangle$ energies, and ratios of kinetic to magnetic $\langle E_k/E_m \rangle$ energies along the vortex radius from the center, $r = 0$, to the boundary $r = R$. The radial profiles are shown for vortices #7 (a), (d), (g), #8 (b), (e), (h), and #12 (c), (f), (i) at different heights: $H = 0.1$ Mm (a), (b), (c); $H = 0.3$ Mm (d), (e), (f); $H = 0.5$ Mm (g), (h), (i).

by the evolution of the plasma motion as those changes impact $S_{z,H}$.

3.5. Heating Mechanisms and Vortices

In this section, we evaluate the possible contribution of vortices to other heating mechanisms such as current dissipation and viscous heating. Although this simulation set in particular does not consider physical dissipations, the present analysis provides an important hint on the role of vortical plasma motion in heating processes. Thus, neglecting contributions due to temperature variations (included in the variation of viscosity coefficient and conductivity) and focusing only on the contribution of flows, the viscous heating rate can be written as

$$H_\nu \propto \left[\frac{1}{2} \boldsymbol{\mathcal{S}}_{ij}^2 - \frac{2}{3} (\nabla \cdot \boldsymbol{v})^2 \right], \tag{7}$$

where $\boldsymbol{\mathcal{S}}_{ij} = \partial v_i / \partial x_j + \partial v_j / \partial x_i$ is the strain rate tensor.

Thereby, we computed H_ν, and the current density squared, J^2, in the simulated atmosphere as those quantities are determined by the plasma dynamics rather than being imposed by simulation parameters. The distributions H_ν and J^2 are indicated by their volume rendering depicted in the second and third panels of Figure 10, respectively. The first panel of Figure 10 displays a different field of view from Figure 1. Both H_ν and J^2 are normalized by their maximum values in the atmosphere, and we see that the highest values for those variables are found along the intergranular lanes and in proximity to the detected vortices. The distribution of the viscous heating shows that regions presenting high values of H_ν are mostly found either between vortices or within the vortex tube. Thus, the vortical motion might be an important mechanism to create large values of H_ν in small scales, which could create a favorable condition for plasma heating due to viscous dissipation in line with earlier findings by N. Yadav et al. (2021). The current sheets, indicated by the high values of J^2, tend to decrease their intensity as a function of height. However, although they appear close to vortices, it cannot be directly established that the vortices entirely produce those current sheets as the current can be produced by the high magnetic field gradients in the region, which are only in part created by the vortex tubes.

4. Discussion and Conclusions

In this work, we applied the IVD technique to detect the 3D kinetic vortex tubes in a simulated solar plage region, continuing the work presented in S. S. A. Silva et al. (2020, 2021). The intergranular lanes where the vortices are detected present localized hotter and colder plasma regions, indicating the existence of pressure and density gradients. Our analysis shows that the role of vorticity generation of those gradients, i.e., the cross product of pressure and inverse density

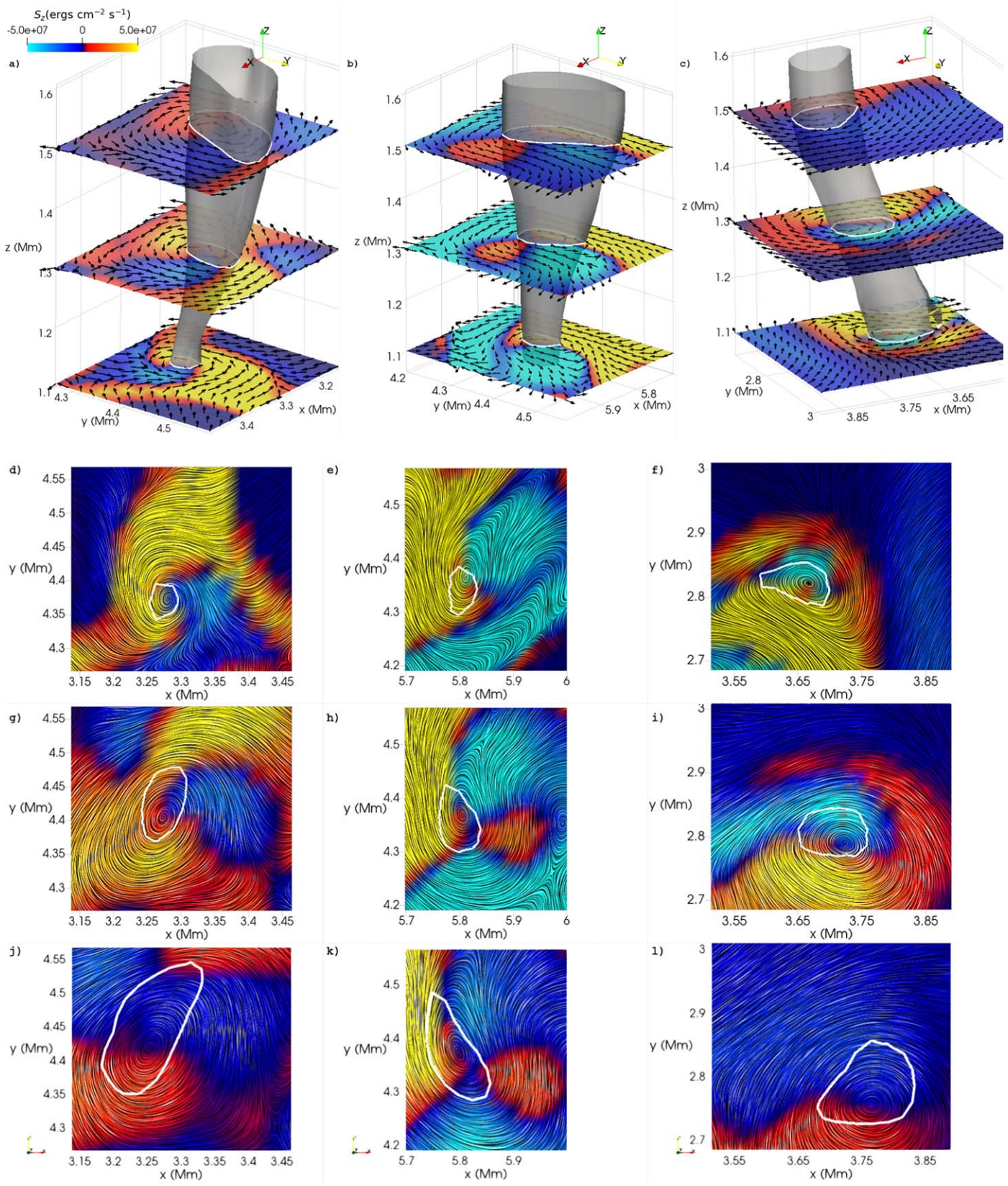

Figure 8. Close view of vortices #7 (a), (d), (g), (j), #8 (b), (e), (h), (k), and #12 (c), (f), (i), (l) at $t = 0$ s. Panels (a), (b), (c): The vortex tube is crossed by x–y planes colored by the z-component of the MHD Poynting flux, S_z, and the black arrows provide the orientation of the horizontal component of the velocity field. Panels (d)–(l): x–y plane placed at $z = 1.1$ Mm (d)–(f); 1.3 Mm (g)–(i); and 1.5 Mm (j)–(l) colored by S_z and the velocity field direction indicated by the LIC. The white contour indicates the vortex boundary at each height level.

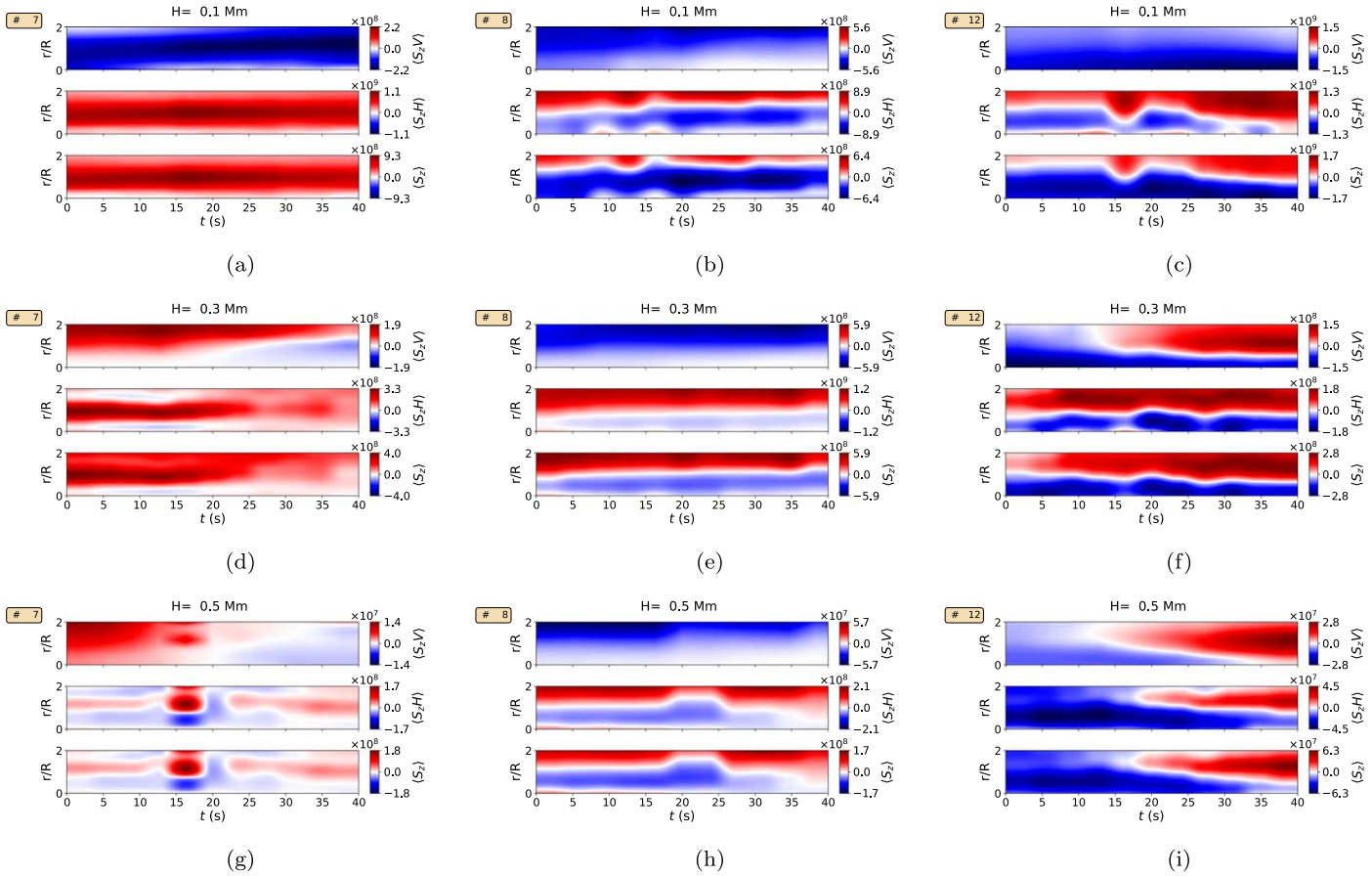

Figure 9. The average S_{zV}, S_{zH}, and S_z along the vortex radius from the center, $r = 0$, to the boundary $r = R$. The radial profiles are shown for vortex #7 (a), (d), (g), #8 (b), (e), (h), and #12 (c), (f), (i) at different heights: $H = 0.1$ Mm (a), (b), (c); $H = 0.3$ Mm (d), (e), (f); $H = 0.5$ Mm (g), (h), (i).

gradients, is negligible compared to the ones provided by the magnetic terms inside the vortex tubes. This is caused by the alignment of those gradients in the vortex region, leading to low values of the baroclinic term, $T2$.

The dominance of the magnetic terms in generating vorticity is in accordance with the analysis performed by S. Shelyag et al. (2011), where they analyzed the contribution for vorticity of all four terms. The difference is that their analysis was based on horizontal averages over the domain. Their results indicate that vorticity in the upper domain is mainly generated by the term concerning the magnetic tension, $T4$. For the regions close to the surface, they found a more significant contribution from the term representing the hydrodynamic baroclinic effects. On the other hand, our results only concern the evolution of vorticity within coherent vortices, that is, due to stable rotational flow. The dominance of magnetic baroclinic and magnetic tension terms for vorticity generation is also an indication that it is very unlikely that the vortices are generated by Kelvin–Helmholtz instability as found by I. N. Kitiashvili et al. (2012) for radiative hydrodynamic simulations. Moreover, the terms $T3$ and $T2$ can create vorticity in opposite directions, indicating that the magnetic field might be acting by suppressing the development of that instability. Our results show that the vorticity evolution of photospheric coherent vortex tubes is mainly created by the misalignment between the gradients of inverse density and magnetic pressure and can be approximated by Equation (3). Therefore, our results suggest that the magnetic field plays an important role for the vorticity evolution of lasting vortex tubes.

The presence of strong temperature gradients is also present inside the vortices. Both high and low-temperature plasma regions are attracted into the vortex tube, leading to plasma mixing within the vortex. As a result, we find that the plasma temperature at the vortex centers as a function of height tends to vary in time, with the majority of vortices experiencing cooling. Those temperature–height profiles indicate distinct heating and cooling rates for plasma at different heights. The averaged radial profiles show a similar temporal evolution and spatial distribution within the vortex tube for the pressure, density, and temperature. For most of the cases, the average density radial distribution shows the vortex is being depleted as the result of the Lorentz force pushing plasma out of the vortex against the pressure gradient force. Moreover, our result suggest that the colder and hotter temperature regions in the upper part of the simulation domain correspond to the areas where the Lorentz force acts, expanding or compressing the plasma, respectively. This implies that the work done by Lorentz force is contributing to the plasma adiabatic cooling and heating in the regions surrounding and inside vortex tubes.

The forces acting on the vortices also lead to variations in the velocity components (S. S. A. Silva et al. 2020; Y. Aljohani et al. 2022), causing changes in kinetic energy as a function of time. The average density and tangential velocity radial profile (S. S. A. Silva et al. 2020) lead to higher kinetic energy at the vortex boundary, as was also obtained by I. N. Kitiashvili et al. (2012). The observed variation of internal energy inside the vortex tubes is caused by either heating or kinetic energy being reverted into internal energy by the work of plasma expansion

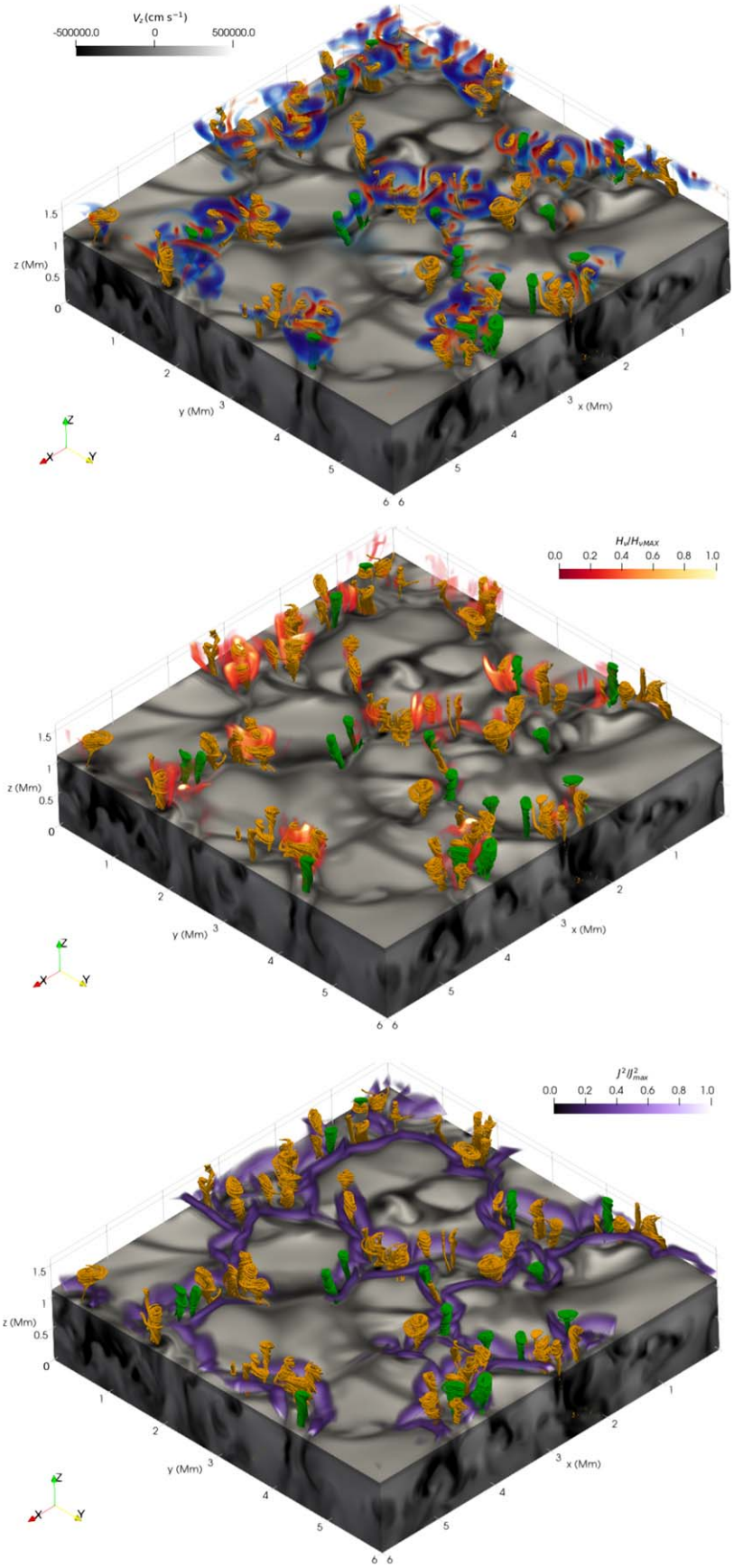

Figure 10. First panel is the same as Figure 1 in a different perspective. The second (third) panel shows the vortices immersed in the volume rendering of the normalized viscous heating (squared current density).

with height. As the vortical motion attracts magnetic field lines (I. S. Requerey et al. 2018; S. S. A. Silva et al. 2020; A. C.-L. Chian et al. 2022), it increases the magnetic energy inside the vortex. The ratio E_k/E_m is always less than unity, indicating that vortices create more magnetic than kinetic energy. Also, as E_k/E_m is not constant and small, it hints that any dynamic turbulence created by vortical motions would be magnetic helicity dominated (e.g., D. Biskamp 2003). Thereby, the flow vortices act by creating large magnetic structures from the magnetic elements they attract during their lifetime.

The magnetic energy generated by vortex tubes is not uniformly transported by Poynting flux. Although around half of the detected vortices present a negative net vertical flux, the contributions from the vortices are around 1.38×10^8 erg s^{-1} cm^{-2}, which is enough to justify chromospheric temperatures. The Poynting flux inside the analyzed vortices varies in time and is generated mainly by horizontal plasma motions, as found by S. Shelyag et al. (2012), and, therefore, is greatly affected by changes in vortical flows, making vortices highly dynamic energy channels. Despite the magnetic energy being greater at the vortex center, the vertical component of the Poynting flux tends to be higher at the vortex boundary, as also found by I. N. Kitiashvili et al. (2012), and at the vortex surroundings, which indicates that shear might be more effective in creating upflows of magnetic energy. This also contributes to explaining the hotter plasma regions observed between interacting vortices. The areas presenting upflow of Poynting flux tend, in general, to display higher plasma temperatures.

Our findings suggest that vortices can efficiently create large values of viscous heating on small scales in the photosphere, indicating that this particular heating mechanism could be enhanced by vortical motion. This is in accordance with the findings from N. Yadav et al. (2021) and S. S. A. Silva et al. (2024) for vortex regions. As the vortex motion impacts the geometry of magnetic field lines, e.g., S. S. A. Silva et al. (2020, 2021) and Y. Aljohani et al. (2022), the plasma rotation might also influence current creation, helping the intensification of the Lorentz force around the vortex region, which in turn may lead to enhanced adiabatic cooling or heating. In summary, our results suggest that photospheric vortex tubes are dynamical electromagnetic energy channels that may also enhance the main plasma heating mechanisms in the photosphere.

Acknowledgments

S.S.A.S., V.F., G.V., and E.R. are grateful to The Royal Society, the International Exchanges Scheme, and collaboration with Brazil (IES\R1\191114). V.F., G.V., and I.B. are grateful to the Science and Technology Facilities Council (STFC) grants ST/V000977/1 and ST/Y001532/1, and to The Royal Society, International Exchanges Scheme, collaboration with Greece (IES/R1/221095) and India (IES/R1/211123). V.F. would like to thank the International Space Science Institute (ISSI) in Bern, Switzerland, for the hospitality provided to the members of the team on "The Nature and Physics of Vortex Flows in Solar Plasmas" and the Institute for Space-Earth Environmental Research (ISEE, International Joint Research Program, Nagoya University, Japan). E.L.R. acknowledges Brazilian agencies CAPES and CNPq (grants 88887.309065/2018-01 and 306920/2020-4, respectively) for their financial support. This research has also received financial support from the European Union's Horizon 2020 research and innovation program under grant agreement No. 824135 (SOLARNET). This research was undertaken with the assistance of resources and services from the National Computational Infrastructure (NCI), which is supported by the Australian Government.

ORCID iDs

Suzana S. A. Silva https://orcid.org/0000-0001-5414-0197
Gary Verth https://orcid.org/0000-0002-9546-2368
Istvan Ballai https://orcid.org/0000-0002-3066-7653
Erico L. Rempel https://orcid.org/0000-0002-4971-5854
Sergiy Shelyag https://orcid.org/0000-0002-6436-9347
Luiz A. C. A. Schiavo https://orcid.org/0000-0002-5082-1398
Viktor Fedun https://orcid.org/0000-0002-0893-7346

References

Aljohani, Y., Fedun, V., Ballai, I., et al. 2022, ApJ, 928, 3
Attie, R., Innes, D. E., & Potts, H. E. 2009, A&A, 493, L13
Balmaceda, L., Vargas Domínguez, S., Palacios, J., Cabello, I., & Domingo, V. 2010, A&A, 513, L6
Battaglia, A. F., Canivete Cuissa, J. R., Calvo, F., Bossart, A. A., & Steiner, O. 2021, A&A, 649, A121
Biskamp, D. 2003, PPCF, 45, 1827
Cabral, B., & Leedom, L. C. 1993, in Proc. 20th Annual Conf. on Computer Graphics and Interactive Techniques (New York: Association for Computing Machinery), 263
Candelaresi, S., Pontin, D. I., Yeates, A. R., Bushby, P. J., & Hornig, G. 2018, ApJ, 864, 157
Canivete Cuissa, J. R., & Steiner, O. 2020, A&A, 639, A118
Cheung, M. C. M., & Cameron, R. H. 2012, ApJ, 750, 6
Chian, A. C.-L., Rempel, E. L., Silva, S. S. A., Bellot Rubio, L., & Gošić, M. 2022, MNRAS, 518, 4930
Chian, A. C. L., Silva, S. S. A., Rempel, E. L., et al. 2019, MNRAS, 488, 3076
Dakanalis, I., Tsiropoula, G., Tziotziou, K., & Kontogiannis, I. 2022, A&A, 663, A94
Finley, A. J., Brun, A. S., Carlsson, M., et al. 2022, A&A, 665, A118
Giagkiozis, I., Fedun, V., Scullion, E., Jess, D. B., & Verth, G. 2018, ApJ, 869, 169
Haller, G., Hadjighasem, A., Farazmand, M., & Huhn, F. 2016, JFM, 795, 136
Iijima, H., & Yokoyama, T. 2017, ApJ, 848, 38
Khomenko, E., Collados, M., Diaz, A., & Vitas, N. 2014, PhPl, 21, 092901
Kitiashvili, I. N., Kosovichev, A. G., Lele, S. K., Mansour, N. N., & Wray, A. A. 2013, ApJ, 770, 37
Kitiashvili, I. N., Kosovichev, A. G., Mansour, N. N., & Wray, A. A. 2012, ApJ, 751, L21
Kleimann, J., & Hornig, G. 2001, SoPh, 200, 47
Kuridze, D., Zaqarashvili, T. V., Henriques, V., et al. 2016, ApJ, 830, 133
Moll, R., Cameron, R. H., & Schüssler, M. 2011, A&A, 533, A126
Moll, R., Cameron, R. H., & Schüssler, M. 2012, A&A, 541, A68
Requerey, I. S., Cobo, B. R., Gošić, M., & Bellot Rubio, L. R. 2018, A&A, 610, A84
Shelyag, S., Keys, P., Mathioudakis, M., & Keenan, F. P. 2011, A&A, 526, A5
Shelyag, S., Mathioudakis, M., & Keenan, F. P. 2012, ApJL, 753, L22
Shetye, J., Verwichte, E., Stangalini, M., et al. 2019, ApJ, 881, 83
Silva, S. S. A., Fedun, V., Verth, G., Rempel, E. L., & Shelyag, S. 2020, ApJ, 898, 137
Silva, S. S. A., Verth, G., Rempel, E. L., et al. 2021, ApJ, 915, 24
Silva, S. S. A., Verth, G., Rempel, E. L., et al. 2024, ApJ, 963, 10
Skirvin, S., Verth, G., González-Avilés, J. J., et al. 2023, AdSpR, 71, 1866
Snow, B., Fedun, V., Gent, F. A., Verth, G., & Erdelyi, R. 2018, ApJ, 857, 125
Tziotziou, K., Scullion, E., Shelyag, S., et al. 2023, SSRv, 219, 1
Tziotziou, K., Tsiropoula, G., & Kontogiannis, I. 2019, A&A, 623, A160
Tziotziou, K., Tsiropoula, G., Kontogiannis, I., Scullion, E., & Doyle, J. G. 2018, A&A, 618, A51
Vögler, A., Shelyag, S., Schüssler, M., et al. 2005, A&A, 429, 335
Wedemeyer-Böhm, S., Scullion, E., Steiner, O., et al. 2012, Natur, 486, 505
Yadav, N., Cameron, R. H., & Solanki, S. K. 2021, A&A, 645, A3
Yuan, Y., de Souza e Almeida Silva, S., Fedun, V., Kitiashvili, I. N., & Verth, G. 2023, ApJS, 267, 35